Characterization of Methane/Cryogenic Oxygen Non-Premixed Rotating Detonation

Qingyang Meng, Chihyung Wen
Department of Aeronautical and Aviation Engineering, The Hong Kong Polytechnic University
Hung Hom, Kowloon, Hong Kong

1 Introduction

Rotating detonation engine (RDE) is a promising technology to fulfill the increasing interest in space exploration because its potential for self-pressurization and compact heat liberation processes [1, 2]. Research efforts have been made on heterogeneous RDE featured by multiphase reacting flow, in which the presence of droplet satisfies the compact requirements for space aircraft [3], while it reduces the detonation sensitivity in liquid-fueled rotating detonation due to the involved evaporation and breakup of fuel droplets [4, 5]. For stabilizing liquid-fueled detonation, reactant is generally preheated to promote evaporation and facilitate detonation propagation. In contrast, heterogeneous rotating detonation in the mixture consisting of gaseous fuel and liquid oxidant at cryogenic temperature, remains sensitive to detonation and suitable for detonation applications. The introduced cryogenic oxidant droplets keep high evaporation rate at room temperature before impacted by the rotating detonation wave, which improves the stability of detonation. Extant studies on rotating detonation fed with liquid oxidant at cryogenic temperature are limited, and they concentrate on detonation transition in a tube [6, 7].

In this study, non-premixed RDE fed with gaseous methane (GCH_4) and liquid oxygen (LO_2) in a two-dimensional configuration is simulated with Eulerian−Lagrangian method. We aim to address the characterization and dynamics of rotating detonation when it propagates across the heterogeneous GCH_4/LO_2 mixture. Shock−droplet interactions in the vicinity of detonation front are elucidated.

2 Numerical setup and physical configuration

2.1 Governing equation

For continuous phase, the equations of mass, momentum, energy, and species mass fraction have been illustrated in our previous work [5, 8], and they are not repeated for brevity. The governing equations of mass, momentum, and energy for liquid phase read

$$\frac{\mathrm{d}m_d}{\mathrm{d}t} = -\dot{m}_d, \tag{1}$$

Correspondence to: chihyung.wen@polyu.edu.hk

$$\frac{\mathrm{d}\mathbf{U}_d}{\mathrm{d}t} = \frac{\mathbf{F}_{d,s} + \mathbf{F}_{d,p}}{m_d}, \tag{2}$$

$$c_{p,d}\frac{\mathrm{d}T_d}{\mathrm{d}t} = \frac{\dot{Q}_c + \dot{Q}_{lat}}{m_d}, \tag{3}$$

where t is time, $m_d = \pi\rho_d d^3/6$ is the droplet mass, ρ_d and d are the droplet density and diameter, respectively. $\mathbf{U}_d$ is the droplet velocity vector, $c_{p,d}$ is the droplet heat capacity, and T_d is the droplet temperature. The droplet evaporation rate in Eq. (1) is determined by

$$\dot{m}_d = \pi d Sh D_{ab}\rho_s \ln(1 + X_r), \tag{4}$$

where Sh is the Sherwood number, D_{ab} the vapor diffusivity in the gaseous mixture, ρ_s the vapor density at the droplet surface, and $X_r = (X_s - X_c)/(1 - X_s)$ is the molar ratio estimated from the condensed species in the surrounding gas and fuel species at the droplet surface. X_c is the molar fraction of condensed species in the surrounding gas, and X_s is the fuel species molar fraction at the droplet surface. The droplet boiling process is not considered in this study. The Stokes drag ($\mathbf{F}_{d,s}$) and pressure gradient force ($\mathbf{F}_{d,p}$) are considered in the droplet momentum equation. They read $\mathbf{F}_{d,s} = m_d(18\mu_d/\rho_d d^2)(C_d Re_d/24)(\mathbf{U_c} - \mathbf{U_d})$ and $\mathbf{F}_{d,p} = -1/6\pi d^3\nabla p$, respectively. μ_d is the dynamic viscosity of the liquid, and C_d is the drag coefficient, estimated with the Schiller and Naumann model. Re_d is the droplet Reynolds number, p the pressure, and $\mathbf{U_c}$ the gas velocity vector at the droplet position. In Eq. (3), $\dot{Q}_c$ is the convective heat transfer rate, i.e., $\dot{Q}_c = h_c A_d(T - T_d)$, where h_c is the heat transfer coefficient, following Ranz and Marshall model with the Bird Correction method [9]. A_d represents the droplet surface area, and T is the gas temperature. Droplet breakup is modelled following Reitz and Diwakar [10, 11], and the droplet diameter change rate (η) follows

$$\eta = \frac{\mathrm{d}d}{\mathrm{d}t} = -\frac{d - d_s}{\tau_b}, \tag{5}$$

where d_s is the maximum stable diameter. τ_b is the breakup time, which is calculated based on the bag and striping breakup regimes, respectively.

2.2 Physical problem

Two-dimensional rectangular configuration with streamwise length of 0.25 m and spanwise length of 0.05 m is used, as displayed in Fig. 1. The left and right boundaries are periodic. The upper outlet is non-reflective. Gaseous methane at room temperature is injected from the lower boundary with mass flow rate of 0.286 kg/s. We assume that the primary atomization has finished in cone injector, and hence monodispersed cryogenic oxygen sprays with temperature of 106 K and initial diameter (d_0) of 30−100 μm, are introduced by 12 cone injectors evenly distributed along the methane inlet. The cone injector angle is 45 degree. Detonation is initialized by one hotspot (20 atm and 3,000 K) on the leftmost boundary, which ignites the gaseous CH_4/O_2 premixture layer with equivalence ratio of 0.3. The computational domain is discretized by 625,000 meshes. Specifically, uniform mesh size of 0.1 mm is distributed in streamwise direction, while in spanwise direction, its size stretches from 0.05 mm at inlet end to 0.5 mm at outlet end. This allows to capture details of detonation height with appropriate meshes.

The Eulerian−Lagrangian method considering gas-droplet two-way coupling is adopted to solve the compressible reactive two-phase flows by the solver *RYrhoCentralFoam*, which has been validated in Ref. [12]. The flow is treated as ideal because the cryogenic oxygen droplets are surrounded by the gaseous methane at room temperature, and the average pressure in the combustor is far lower than oxygen critical value. For the Eulerian phase, a second-order implicit backward method is employed for temporal discretization. The timestep is adjustable with the maximum Courant number less than 0.1, and the time step is around 10^{-9} s. The second-order upwind-central scheme is applied to the convective

terms in the momentum equations. The methane chemical mechanism includes 17 species and 44 reactions [13]. The droplet equations are solved with a first-order implicit Euler method.

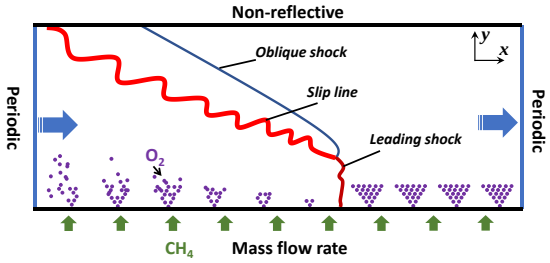

Figure 1: Schematic of computational domain.

3 Results and discussion

3.1 Evolution and dynamic

Evolution of detonation mode is visualized by the detonation surface plot in Fig. 2, in which the pressure trace along streamwise direction at a height of 10 mm is tracked as a function of time. The high pressure demonstrates the detonation front. When d_0 = 30 μm, attenuated detonation with low pressure peak is observed during 180 μs−300 μs, characterized with discontinuous peak pressure trace in Fig. 2(a). Subsequently, detonation recovers with amplified pressure at wavefront. This transient process after initiation results from the detonation transition from gaseous premixture in the first cycle to inhomogeneous GCH_4/LO_2 mixture in the second cycle. The second detonation wavefront appears at around 350 μs and co-rotating detonation mode is established. Detonation mode progressively stabilizes afterwards with a speed of around 1740 m/s. As d_0 increases to 100 μm, single-wave mode can be identified in Fig. 2(b) with slightly low speed of 1703 m/s, and the blurred peak trace demonstrates the presence of chaotic pressure due to the extended breakup and evaporation time.

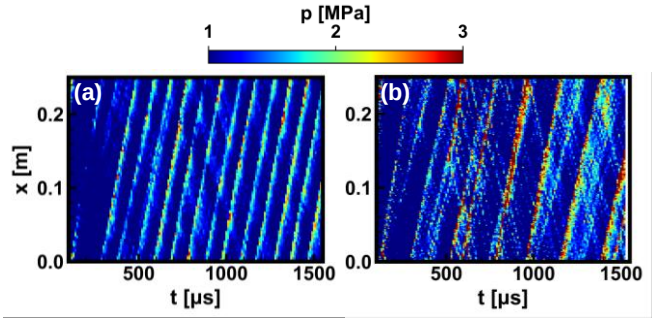

Figure 2: Detonation surface plot: (a) d_0 = 30 μm, (b) d_0 = 100 μm. The surface plot is constructed using the pressure trace at a height of 10 mm.

The formation of detonation mode with d_0 = 30 μm is illustrated as the representative case by displaying the time sequence of temperature and heat release rate (HRR) contours, as seen in Fig. 3. At 0.00011 s, strong detonation evidenced by distinct leading shock, approaches the rightmost boundary in the first cycle. It couples with the reaction front featured with high HRR, as seen in Fig. 3(f). Detonation is attenuated with faint HRR at 0.00018 s in the second cycle, and it is strengthened progressively. Secondary co-rotating detonation wave appears at 0.00035 s, as indicated in Fig. 3(d), while this newborn detonation leads to minor chemical heat release; see Fig. 3(i). At 0.00167 s, after around 8 cycles, co-rotating detonation mode has been stabilized.

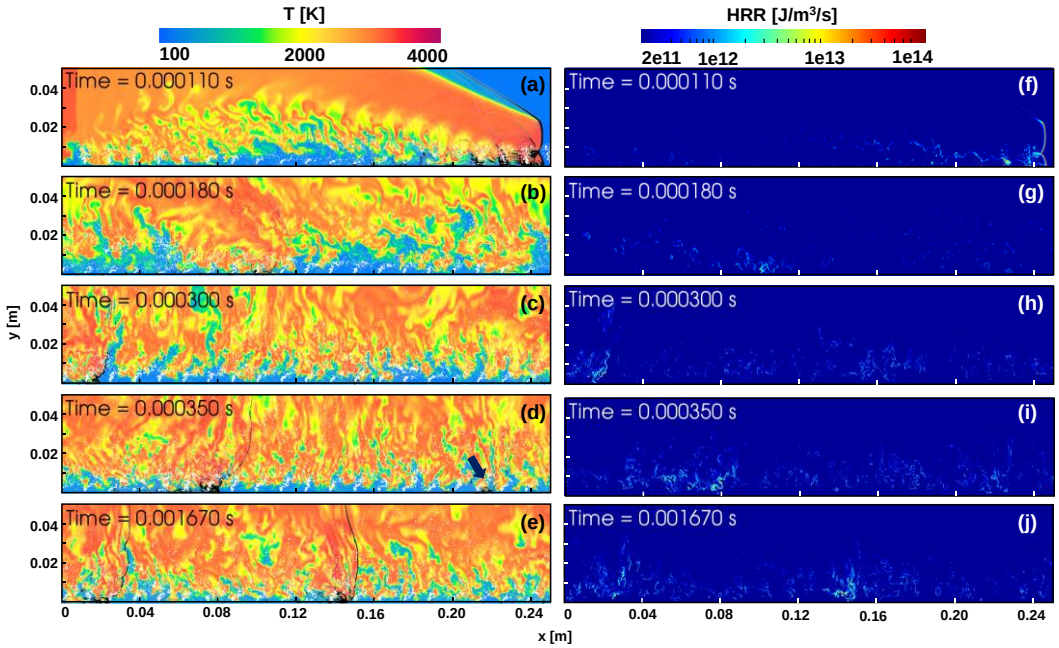

Figure 3: Time sequence of (1st column) temperature and (2nd column) HRR contours. White scatters in temperature contours are oxygen droplets, and pressure gradient magnitude is overlaid.

3.2 Detonation structure and droplet behavior

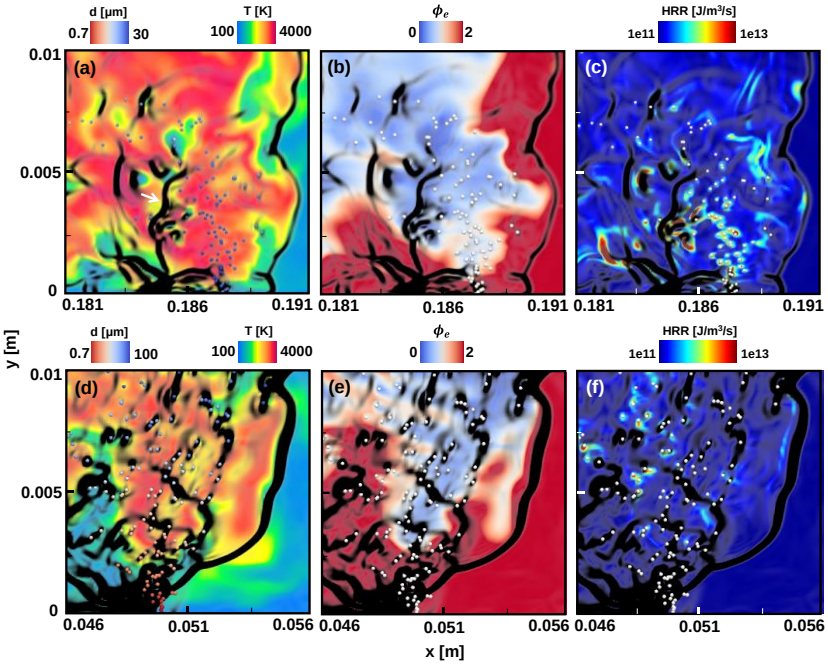

Figure 4: Detonation structure: contours of (a) temperature, (b) HRR, and (c) effective ER at d_0 = 30 μm (1st row) and d_0 = 100 μm (2nd row). Droplets are colored by diameter in (a) and (d). Pressure gradient magnitude is overlaid.

Detonation structure is displayed by the zoomed view in the vicinity of leading shock when d_0 = 30 and 100 μm, as shown in Fig. 4. The effective equivalence ratio ϕ_e is calculated from an element-based definition [14], i.e., the ratio of required stoichiometric oxygen atoms to the available oxygen atoms. For d_0 = 30 μm, one cluster of oxygen sprays introduced from the injector is impacted by detonation.

In Fig. 4(a), nonuniform temperature behind detonation front is observed, which results from the inhomogeneity in effective ER as seen in Fig. 4(b). Strong shocks in post-shock area are induced by the local explosion where elevated HRR at locations of oxygen droplets is found, as seen in Fig. 4(c). In addition, the high HRR and fast chemistry leads to the shocklets in the vicinity of droplets, which differs from the liquid-fueled detonation. Similarities are observed when d_0 = 100 μm. Due to the extended breakup and evaporation time of large oxygen droplets, temperature in post-detonation area is comparatively low as seen in Fig. 4(d). In addition, the minor evaporation rate results in the high ϕ_e and faint local HRR near oxygen droplet, as shown in Figs. 4(e) and 4(f).

Figure 5 displays the relationship between Weber number (We) and evaporation rate of Lagrangian droplet ($\dot{m}$). p_c is the pressure of continuous phase at droplet position. Here, $We \equiv \rho_c(\mathbf{U}_c - \mathbf{U}_d)^2 d/\sigma$, where σ is the surface tension, and ρ_c is the continuous density. For d_0 = 30 μm, the droplets with low We and ρ_c experience minor evaporation, and they correspond to those ahead of detonation front. When $We > 10^3$, most of droplets are in high-pressure environment and the evaporation rates are distributed, which are immediately impacted by detonation front and in post-detonation area. The droplets at detonation front generally have extreme We. Some droplets with elevated evaporation rate reach their boiling point, which locate in post-detonation area or are trapped into deflagration. For d_0 = 100 μm, similar distributions of scatter are found. The increased in droplet size with large surface area leads to substantial evaporation rate, as seen in Fig. 5(b).

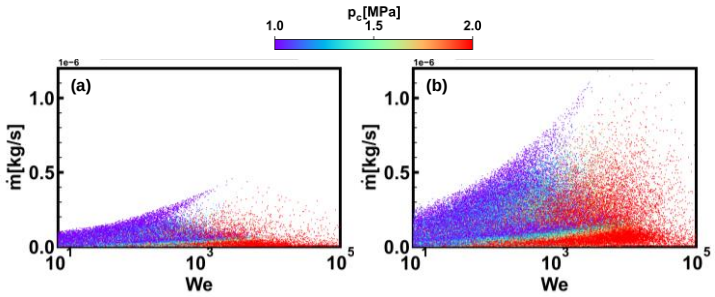

Figure 5: Scatterplots of Weber number and evaporation rate when (a) d_0 = 30 μm and (b) d_0 = 100 μm. Dot is colored by the p_c.

Droplet behavior after introduced into the combustor is monitored by tracing the its diameter, temperature, and Weber number, as seen in Fig. 6. The moment at which droplet is impacted by the detonation is indicated. Once entered into the combustor, the Weber number decreases due to the reduced velocity differences, and the droplet diameter decreases as the fragmentation and evaporation proceed. The competition between heat absorption from phase change and the heating from the hot detonative product, leads to the fluctuations in droplet temperature, while it overall increases. The interaction between droplet and the leading shock is characterized by the peak We, and the followed secondary peak in Fig. 6(b) originates from the chaotic pressure in post-detonation area.

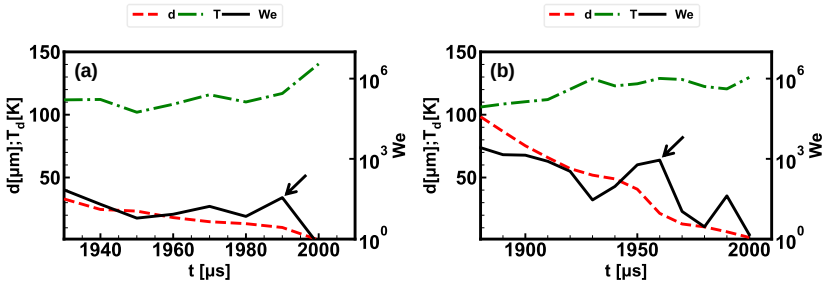

Figure 6: Time-varying parameters of a single oxygen droplet.

4 Conclusion

Evolution and structure of methane/cryogenic oxygen rotating detonation wave under non-premixed injection pattern are simulation in a two-dimensional configuration. Co-rotating detonation mode is observed at d_0 = 30 μm, while single-wave mode is achieved at d_0 = 100 μm. The occurrence of the second detonation wave results from the local high pressure and HRR, which is similar to gas detonation. Elevated HRR is observed at oxygen droplet position immediately behind detonation front due to the fast evaporation rate of oxygen sprays, which leads to local explosion accompanied with some shocklets.

Acknowledgement

This work is supported by Chongqing Postdoctoral Science Foundation (CSTB2022NSCQ-BHX0023).

References

[1] Gray S, McLoughlin M, Ciccarelli G. (2024). Fuel-oxygen mixing and detonation propagation in a linear rotating detonation rocket engine geometry. Combust. Flame 260: 113250.

[2] Prakash S, Bielawski R, Raman V, Ahmed K, Bennewitz J. (2024). Three-dimensional numerical simulations of a liquid RP-2/O2 based rotating detonation engine. Combust. Flame 259: 113097.

[3] Salvadori M, Panchal A, Menon S. (2023). Simulation of liquid droplets combustion in a rotating detonation engine. Proc. Combust. Inst. 39: 3063.

[4] Watanabe H, Matsuo A, Chinnayya A, Itouyama N, Kawasaki A, Matsuoka K, et al. (2023). Lagrangian dispersion and averaging behind a two-dimensional gaseous detonation front. J. Fluid Mech. 968: A28.

[5] Meng Q, Zhao M, Xu Y, Zhang L, Zhang H. (2023). Structure and dynamics of spray detonation in *n*-heptane droplet/vapor/air mixtures. Combust. Flame 249: 112603.

[6] Shen X, Fu W, Liang W, Wen JX, Liu H, Law CK. (2022). Strong flame acceleration and detonation limit of hydrogen-oxygen mixture at cryogenic temperature. Proc. Combust. Inst. 39: 2967.

[7] Kuznetsov M, Denkevits A, Veser A, Friedrich A. (2022). Flame propagation regimes and critical conditions for flame acceleration and detonation transition for hydrogen-air mixtures at cryogenic temperatures. Int. J. Hydrogen Energ. 47: 30743.

[8] Zhao M, Ren Z, Zhang H. (2021). Pulsating detonative combustion in n-heptane/air mixtures under off-stoichiometric conditions. Combust. Flame 226: 285.

[9] Bird RB, Stewart WE, Lightfoot EN. Transport phenomena: John Wiley & Sons; 1960.

[10] Reitz RD, Diwakar R. (1986). Effect of drop breakup on fuel sprays. SAE Trans. 95: 218.

[11] Reitz RD, Diwakar R. (1987). Structure of high-pressure fuel sprays. SAE Trans. 96: 492.

[12] Huang Z, Zhao M, Xu Y, Li G, Zhang H. (2021). Eulerian-Lagrangian modelling of detonative combustion in two-phase gas-droplet mixtures with OpenFOAM: Validations and verifications. Fuel 286: 119402.

[13] Monnier F, Ribert G. (2022). Simulation of high-pressure methane-oxygen combustion with a new reduced chemical mechanism. Combust. Flame 235: 111735.

[14]Zhou R, Hochgreb S. (2013). The behaviour of laminar stratified methane/air flames in counterflow. Combust. Flame 160: 1070.